Post-Print of an Accepted Manuscript on the Laboratory of Turbulent Flows Website

The Accepted Manuscript begins on the next page.

The mode B structure of streamwise vortices in the wake of a two-dimensional blunt trailing edge

Bradley Gibeau[1] and Sina Ghaemi[1]†

[1]Department of Mechanical Engineering, University of Alberta, Edmonton, Alberta T6G 2R3, Canada

The structure of streamwise vortices that arises due to secondary instabilities in the wake of a two-dimensional blunt body with a chord to thickness ratio of 12.5 was investigated using high-speed stereoscopic particle image velocimetry. Reynolds numbers spanning an order of magnitude from $Re(h) = 2600$ to 25800 were considered, where h is the height of the blunt trailing edge. A modified two-dimensional Q-criterion ($Q' = \omega_x Q/|\omega_x|$) was applied to identify the streamwise vortices. The wavelength of the streamwise vortices, defined as the spanwise distance between adjacent streamwise vortex pairs in the wake, was investigated by applying an autocorrelation algorithm to snapshots of Q'. The most probable wavelength was found to range from $0.67h$ to $0.85h$ with increasing Re, and the mean wavelengths increased from $0.77h$ to $0.96h$. These wavelength values appeared to increase asymptotically. Visual inspection and cross-correlation analyses based on Q' showed that the streamwise vortices maintain their directions of rotation during primary shedding cycles. The latter analysis was carried out at low Re because of a large amount of wake distortion and the absence of time-resolved data at high Re. The characteristics of the streamwise vortex structure found here match those of mode B, which, at similar Re, dominates the wakes of circular and square cylinders and has also recently been shown to exist in the wake of an elongated blunt body with a larger chord to thickness ratio of 46.5 (Gibeau *et al., J. Fluid Mech.*, vol. 846, 2018, pp. 578–604).

1. Introduction

Understanding the dynamics of bluff body flows is vital to the design and improvement of a variety of systems. For example, road, marine, and aerospace vehicles often feature bluff body geometries due to practical requirements. The result is flow separation at the rear of the body, leading to a complex, low-pressure wake. Many of these bluff bodies feature trailing edge geometries that allow for variable separation points. The simplest example of such a geometry is the circular cylinder, which has been used extensively in the study of bluff body wakes. When the trailing edge of a bluff body is blunted, the separation points become fixed, resulting in slightly different wake behaviour. The wakes of blunted bluff bodies have not received as much attention but still remain important

† Email address for correspondence: ghaemi@ualberta.ca

to a variety of applications. For example, an airfoil with a blunt trailing edge (BTE) is beneficial to the design of wind turbine blades (Standish & van Dam 2003; Baker *et al.* 2006). The secondary instabilities in the wake of a nominally two-dimensional BTE, which have been the subject of contradictory studies as of late, are the topic of the present work. These instabilities influence the organization of streamwise vortices in the wake, and recent experimental works have reported different conclusions regarding their scale (Naghib-Lahouti *et al.* 2012, 2014; Gibeau *et al.* 2018). These works will be further discussed shortly.

The primary instability in the wake of a two-dimensional bluff body is of the von Kármán type and results in the shedding of large, spanwise vortices from the trailing edge in an alternating fashion. These spanwise vortices have been well-documented for decades and have been the subject of multiple review papers, for example those of Berger & Wille (1972), Oertel (1990), and Williamson (1996*b*). The secondary instabilities are less well-documented and less well-understood, and they manifest as concentrations of streamwise vorticity in the wake. More specifically, the secondary instabilities take the form of streamwise vortex pairs that are interwoven with the von Kármán vortices. After two early investigations revealed evidence of secondary instabilities (Gerrard 1978; Wei & Smith 1986), Williamson (1988) showed that the wake of a circular cylinder transitions through two Reynolds number-dependant secondary instability modes, which he referred to as mode A and mode B. This discovery spurred numerous investigations into the secondary instabilities in the wakes of cylinders in the following decade which confirmed and further characterized both mode A (Zhang *et al.* 1995; Brede *et al.* 1996; Williamson 1996*a*) and mode B (Bays-Muchmore & Ahmed 1993; Mansy *et al.* 1994; Zhang *et al.* 1995; Brede *et al.* 1996; Williamson 1996*a*; Wu *et al.* 1996). The following descriptions of modes A and B are derived from the results of these studies.

The circular cylinder mode A features streamwise-aligned vortices that exist in pairs. The vortices change their direction of rotation every half-shedding cycle of the primary instability and therefore exist in an out-of-phase arrangement. The wavelength of mode A, which is defined as the spanwise distance between adjacent vortex pairs, is roughly $3d$–$5d$ where d is the diameter of the circular cylinder. Mode A has the potential to exist approximately in the Reynolds number range $180 \leqslant Re(d) \leqslant 250$, beginning when the vortex shedding first becomes three-dimensional. There is strong evidence that mode A forms as a result of and is maintained by an elliptic instability (Thompson *et al.* 2001). The mode B structure replaces mode A and exists in the wake for $Re(d)$ spanning several orders of magnitude. In contrast to mode A, the streamwise vortex pairs of mode B have a wavelength of approximately $1d$ and they maintain their directions of rotation during the primary shedding cycles. Jethani *et al.* (2018) recently performed a stability analysis on the near-wake of a circular cylinder and proposed a possible mechanism governing the emergence of mode B. Their work reveals that the origin of mode B is still an active research question. The wakes of square cylinders, which feature a BTE, have been shown to be affected by modes A and B as well. This has been achieved using both stability analysis (Robichaux *et al.* 1999; Blackburn & Lopez 2003; Sheard *et al.* 2009) and through experiments (Luo *et al.* 2007; Tong *et al.* 2008).

A third mode has been predicted by stability analysis to exist in the wakes of circular and square cylinders. This mode was first predicted by Barkley & Henderson (1996) and has been referred to as mode S (Robichaux *et al.* 1999) or mode QP (Blackburn & Lopez 2003; Blackburn *et al.* 2005). The discrepancy between nomenclature originates from the fact that the mode was originally thought to be a subharmonic (S), but was later shown to be quasi-periodic (QP) and will therefore be referred to as mode QP moving forward. Mode QP has an intermediate wavelength that lies between those of modes A and B, and

a unique feature of the instability is that its vortex pairs change their direction of rotation after each primary shedding cycle. Finally, square cylinders at angles of incidence have been shown to have the potential to be afflicted by a mode C (Sheard *et al.* 2009; Yoon *et al.* 2010). This mode is related to breaking the symmetry of the wake flow and has also been observed in the wake of a circular cylinder with a wire disturbance in its wake (Yildirim *et al.* 2013) and has been predicted to exist in the wake of a triangular cylinder at incidence (Ng *et al.* 2018).

Circular and square cylinders are defined by a single characteristic length, but this is not sufficient for all bodies that feature a BTE. In the past, researchers have considered elongated bodies with elliptical leading edges and BTEs, which will be referred to as elongated blunt bodies from here forward. For this type of geometry it is necessary to define the aspect ratio of the body as $AR = c/h$ where c is the chord length and h is the height of the BTE. An early Floquet stability analysis of the secondary instabilities in the wakes of elongated blunt bodies was performed by Ryan *et al.* (2005), who studied bodies with $2.5 \leqslant AR \leqslant 17.5$ for $Re(h)$ up to 700. An important conclusion of this study was that AR dictates which secondary modes are the most unstable in the wake. The authors found that mode A was the most unstable for AR smaller than 7.5, but the first mode to become unstable changed to what they referred to as mode B$'$ as AR was increased past 7.5. Mode B$'$ behaves like mode B, but with a larger wavelength of approximately $2.2h$ and differences in the near-wake vorticity field. A second new mode was also predicted, which they referred to as mode S$'$ for its similarities with the square cylinder mode S (QP). The streamwise vortex pairs of mode S$'$ change their direction of rotation every primary shedding cycle and have a wavelength similar to that of mode B ($\sim 1h$). Mode S$'$ was predicted to be more unstable than mode A for $AR = 17.5$.

Few experimental studies have investigated the streamwise vortices in the wakes of elongated blunt bodies. Naghib-Lahouti *et al.* (2012, 2014) studied the wake of an elongated blunt body with $AR = 12.5$ for $250 \leqslant Re(h) \leqslant 5 \times 10^4$ using a combination of laser-induced fluorescence and particle image velocimetry (PIV). In agreement with Ryan *et al.* (2005), they concluded that streamwise vortex pairs consistent with the mode B$'$ secondary instability existed in the wake with wavelengths ranging from $2.0h$–$2.5h$. However, their analysis did not rely on direct measurements of the streamwise vortices, but on a reduced-order representation of PIV snapshots of streamwise velocity in the streamwise-spanwise plane of the wake, which was achieved using proper orthogonal decomposition (POD). This was possible following the work of Mansy *et al.* (1994) and Wu *et al.* (1996), who showed that the wavelength of the streamwise vortices matches the wavelength of streamwise velocity undulations in the near-wake. As was shown by Gibeau *et al.* (2018), this analysis technique coupled with POD has the potential to greatly skew the wavelength results. Gibeau *et al.* (2018) used PIV to study the streamwise vortices in the wake of an elongated blunt body with a much larger AR of 46.5 for $3500 \leqslant Re(h) \leqslant 7000$. Their analysis compared direct, time-resolved measurements of the streamwise vortices in the wake to the methods of Naghib-Lahouti *et al.* (2012, 2014). It was shown that the use of POD misrepresents the structure of streamwise vortices when applied to streamwise velocity fields in the wake, and that the near-wake undulations in streamwise velocity only match the streamwise vortices when POD is not applied to the velocity fields beforehand. Considering direct measurements of the streamwise vortices and their temporal behaviour, Gibeau *et al.* (2018) concluded the presence of mode B in the wake for a larger AR, and this was in contrast to the results of Naghib-Lahouti *et al.* (2012, 2014). To our knowledge, no further experimental work regarding the streamwise vortices in the wakes of elongated blunt bodies has been carried out.

While Gibeau *et al.* (2018) showed that the analysis technique used by Naghib-Lahouti

et al. (2012, 2014) may have been flawed, the difference in AR between these two studies is too large to draw a conclusion for the lower AR investigated by Naghib-Lahouti *et al.* (2012, 2014) and Ryan *et al.* (2005). The present work seeks to remedy this by utilizing direct measurements of the streamwise vortices, i.e. the same measurement and analysis techniques used by Gibeau *et al.* (2018), to study the structure of streamwise vortices in the wake of a body with $AR = 12.5$, thus matching the geometry used by Naghib-Lahouti *et al.* (2012, 2014). The direct, time-resolved measurements of the streamwise vortices in the wake are used to qualitatively and quantitatively characterize the streamwise vortex structure for $Re(h)$ spanning an order of magnitude. First, the upstream boundary layer is analyzed to account for any effects its transition may have on the wake organization. Next, the characteristics of the spanwise vortices are compared to those reported by Naghib-Lahouti *et al.* (2012, 2014) for validation purposes. The wavelength of the streamwise vortices is then determined by applying an autocorrelation technique to fields of two-dimensional Q-criterion. To characterize the temporal behaviour of the streamwise vortices, visual inspection and cross-correlation analyses are used to determine whether the streamwise vortex pairs maintain their directions of rotation during primary vortex shedding cycles. Finally, all analyses are applied to measurements conducted with and without tripwires added to the model. This is done to further probe the effect of the upstream laminar to turbulent transition on the streamwise vortex structure, as well as the impact of a thicker upstream boundary layer as an input to the wake.

2. Experimental set-up

The wake and upstream boundary layer of an elongated blunt body with $AR = 12.5$ have been investigated using several particle image velocimetry (PIV) experiments. The wake was measured using two-component PIV (2C-PIV) and stereoscopic PIV (stereo-PIV). The upstream boundary layer was measured using 2C-PIV only. A combination of 2C-PIV and hotwire measurements was also used to determine the quality of the flow in the wind tunnel just upstream from the test location. Ten freestream velocities ranging from 3.1 to 31.2 m s^{-1} were considered, corresponding to Reynolds numbers ranging from $Re(h) = 2600$ to 25800 where h is the height of the blunt trailing edge (BTE). All experiments were performed with and without tripwires added to the blunt model $0.23c$ downstream from the leading edge where c is the chord length to investigate their impact on the results.

2.1. *Wind tunnel facility and flow quality*

A two-storey, closed-loop wind tunnel capable of freestream velocities up to 35 m s^{-1} was used for the present experiments. The test section of the wind tunnel has dimensions of $2.4 \times 1.2 \times 11$ m^3 ($W \times H \times L$). Honeycombs, several screens, and a 6.3:1 contraction are used to condition the flow. The test section features clear acrylic walls, and the floor and ceiling are fit with windows for further optical access. The present experiments were conducted approximately 6 m downstream from the end of the contraction.

A 2C-PIV experiment was used to measure the uniformity of the test section within a field-of-view (FOV) denoted as FOV1 located roughly 2 m upstream from the blunt model at the centre of the test section as shown schematically in figure 1(a). The experiment utilized a high-speed camera (Phantom v611) with a 1280×800-pixel CMOS sensor, 20×20 μm^2 pixel size, and 12-bit resolution. A dual-cavity Nd:YLF laser (Photonics Industries DM20-527-DH) provided illumination. The combined beam of the two laser cavities is capable of 40 mJ per pulse at 1 kHz, or the pulses can be alternated to reach frequencies up to 20 kHz with lower energy per pulse. A series of lenses was used
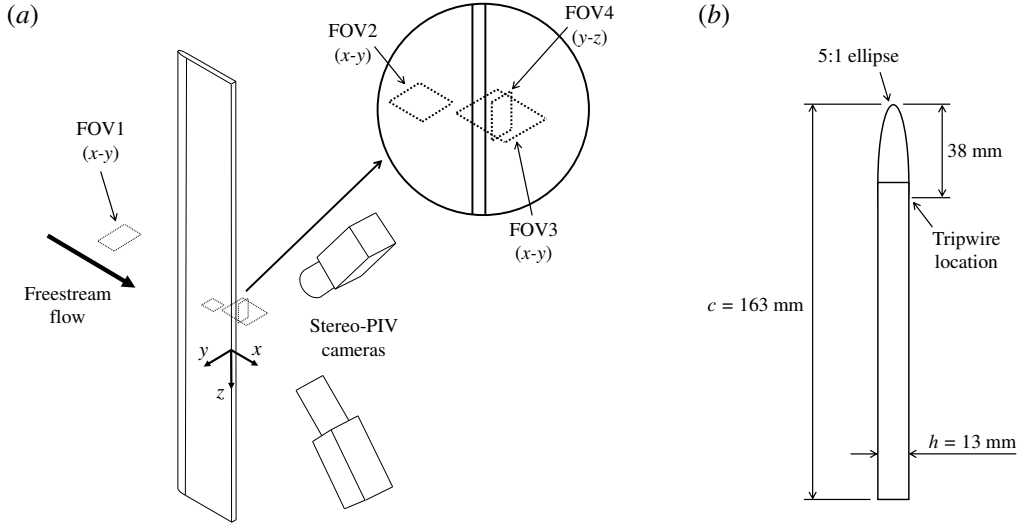
FIGURE 1. Schematics of (*a*) the configurations used for 2C- and stereo-PIV and (*b*) the cross-section of the blunt model with $c/h = 12.5$. The $z = 0$ axis in (*a*) is actually located at centre span; the axis is offset here to not interfere with the fields of view. Note that FOV1 is located roughly 2 m upstream from the model and is shown close to the leading edge here to simplify the schematic.

to create a laser sheet with $\sim$1 mm thickness. A fog generator was used to seed the closed-loop tunnel with $\sim$1 μm particles. A 200-mm Nikon lens with an aperture setting of $f/4$ was used to obtain a FOV of $(\Delta x, \Delta y) = 62 \times 99$ mm^2 ($4.8h \times 7.6h$) with a resolution of 77.4 μm pix^{-1} where x refers to the streamwise direction and y refers to the direction normal to the model surface. Sets of 1000 double-frame images were collected at a frequency of 50 Hz for all freestream velocities considered. The background noise in the images was removed by subtracting the ensemble minimum, followed by normalization using the ensemble average. The images were processed in DaVis 8.4 (LaVision GmbH) using a multi-pass cross-correlation with the final passes utilizing Gaussian 64×64-pixel (5.0×5.0-mm) interrogation windows with 75% overlap. The resulting uncorrelated vector fields were then averaged to obtain mean vector fields for the ten freestream velocities considered.

A hotwire probe (Custom Hot Wires) was used to measure the turbulence intensity of the freestream, defined as the root-mean-square of the freestream velocity fluctuations divided by the mean velocity ($u_{rms}/\langle U \rangle$). The probe was mounted to a rigid arm which extended approximately 50 cm from the leading edge of the blunt model at the centre of the test section. Velocity measurements were conducted at 20 kHz over 10 seconds for each of the freestream velocities considered. Note that the hotwire arm was only connected to the leading edge of the model for these measurements.

The results of the test section uniformity experiment reveal that the flow remains uniform in the y-direction, with the maximum deviation from the mean being 0.5%. The hotwire measurements indicate that the freestream turbulence intensity is 0.5% or lower when the velocity is greater than 5 m/s. These results are consistent with a previous investigation into the flow quality in this wind tunnel by Johnson & Kostiuk (2000), who considered the freestream uniformity and turbulence intensities across the entire height

and width of the test section. The flow quality in the test section is therefore sufficient for the present investigation.

2.2. *Blunt trailing edge model*

The model used in the present experiments was machined from an aluminum plate with a thickness of 13 mm and sanded to a fine surface finish. The model has a chord length of $c = 163$ mm to obtain the desired aspect ratio (AR) of $c/h = 12.5$, and its spanwise length matches the height of the wind tunnel test section (1.2 m). The leading edge was made semi-elliptical with a major to minor axis ratio of 5:1 to prevent upstream flow separation. A schematic of the model cross-section is shown in figure 1(b). The model was oriented vertically at zero angle of attack for all experiments, creating a negligible blockage of 0.5% in the test section. Cylindrical tripwires with a diameter of 1 mm were placed 38 mm ($0.23c$) from the leading edge on both sides of the model for the experiments in which they were used.

The spanwise length of the model corresponds to approximately $94h$. Roughly $82h$ of the model was located in the uniform freestream when the boundary layer growth along the walls of the wind tunnel is considered at the measurement location (at most ~ 8 cm). We therefore do not expect significant wall effects for measurements conducted at the centre of the test section. For comparison, Naghib-Lahouti *et al.* (2012, 2014) conducted experiments on models with spanwise lengths of $34h$ and $27h$, respectively. The work of Gibeau *et al.* (2018) was conducted under the same conditions as the present investigation.

2.3. *Particle image velocimetry of the upstream boundary layer*

The state of the upstream boundary layer and its properties were measured using 2C-PIV within FOV2 at centre-span as shown schematically in figure 1(a). The same laser and camera detailed in section 2.1 were utilized. The laser was used along with a series of optics to create a laser sheet of ~ 1 mm thickness. The camera was fitted with a 200-mm Nikon lens with an aperture setting of $f/4$ to obtain a FOV of $(\Delta x, \Delta y) = 69 \times 43$ mm^2 ($5.3h \times 3.3h$) with a resolution of 53.8 µm pix^{-1}. FOV2 captured the entire boundary layer thickness for all considered cases, and the downstream edge of FOV2 was 1 cm upstream from the BTE. Sets of 2500 double-frame images were collected at a rate of 250 Hz for each of the ten Re, with and without tripwires. The images were preprocessed to improve image quality as described in section 2.1 and DaVis 8.4 was once again used to process the images. An ensemble of correlation (Meinhart *et al.* 2000) was applied to obtain mean velocity fields with higher resolution. A multi-pass cross-correlation was applied with a final interrogation window size of 12×12-pixel (0.65×0.65-mm) with 75% overlap. A 4:1 elliptical Gaussian weighting function was applied to the window with the major axis of the ellipse in the streamwise direction to improve the correlation.

2.4. *Particle image velocimetry of the wake*

The wake was characterized using 2C-PIV and stereo-PIV in FOV3 and FOV4, respectively, as shown schematically in figure 1(a). FOV3 covers an x-y plane and was used to capture the characteristics of the spanwise vortices, and FOV4 covers a y-z plane was used to capture the characteristics of the streamwise vortices. The same high-speed laser and camera detailed in Section 2.1 were utilized in both experiments, with two of the high-speed cameras being used for stereo-PIV.

A 200-mm Nikon lens with an aperture setting of $f/4$ was used to image a ~ 1 mm laser sheet within FOV3 at centre-span. A FOV of $(\Delta x, \Delta y) = 69 \times 43$ mm^2 ($5.3h \times 3.3h$) was

obtained with a resolution of 53.7 µm pix^{-1}. FOV3 captured a small portion of the BTE, which it was centered upon in the y-direction. Sets of 2700 double-frame images were collected for each of the ten Re considered, with and without tripwires, but at different acquisition frequencies. The imaging rate was varied to acquire a long sequence and ensure statistical convergence of the data for determining quantities such as formation length while still being fast enough to measure the vortex shedding frequency. A Strouhal number of $St(h) = 0.2$ was selected using a recent study that considered a similar model in the present wind tunnel (Gibeau *et al.* 2019). This value is similar to that of circular cylinder wakes (Roshko 1954) and what has been found in other investigations of BTE wakes (Petrusma & Gai 1996). It was used to estimate the vortex shedding frequency for each Re, and the imaging rate was chosen to be roughly 4 times this value. This ensured the measurements were acquired at well above the Nyquist frequency for determining the shedding frequency and that more than 600 wake cycles were captured by each data set for statistical convergence. The imaging rates were therefore varied linearly between 200 Hz at $Re(h) = 2600$ and 2 kHz at $Re(h) = 25800$. The images were once again preprocessed as described in section 2.1 and processed in DaVis 8.4. A standard multi-pass cross-correlation was applied on double-frame images with the final passes utilizing Gaussian 32×32-pixel (1.7×1.7-mm) interrogation windows with 75% overlap. Universal outlier detection (Westerweel & Scarano 2005) was applied to some of the high-Re data sets to clean up the resulting vector fields. Less than 5% of the vectors were modified, and they were mostly in the centres of the spanwise vortices where correlation was difficult at these high Re.

Stereoscopic PIV was performed within FOV4, which was centered with respect to the BTE at centre-span. The laser sheet was made to be $\sim$2 mm thick and was located at $x = 2h$ in the wake. Two of the previously mentioned high-speed cameras were fitted with Scheimpflug mounts and 200-mm Nikon lenses and both were situated $\sim$1 m from FOV4 with an angle of $75°$ between their lines of sight. Aperture settings of $f/16$ and $f/8$ were used for the cameras with forward and backward scattering orientation, respectively. A two-step stereoscopic calibration process was used which included a three-dimensional target calibration (i.e. two planes) followed by self-calibration with a set of particle images (Wieneke 2005). The obtained FOV was $(\Delta y, \Delta z) = 52 \times 102$ mm^2 ($4.0h \times 7.8h$) with a resolution of 66.5 µm pix^{-1} and a residual error of 0.02 pix. At each of the ten Re, one uncorrelated and one time-resolved set of images was collected, both with and without tripwires. For the uncorrelated sets, the imaging rates were selected to be just below the estimated shedding frequency to ensure that each snapshot was from a different vortex shedding cycle. The imaging rates were therefore varied linearly between 40 Hz at $Re(h) = 2600$ and 400 Hz at $Re(h) = 25800$ to ensure uncorrelated data sets. The time-resolved data sets were collected in single-frame mode where retaining a correlation was possible, and this was only for the first Re. 5400 single-frame images were collected at 5.0 kHz for $Re(h) = 2600$. High-frequency double-frame mode was used for the remainder of the Re. 2700 double-frame images were collected at 3.1 kHz for $Re(h) = 4900$ to 25800. All images were preprocessed as described in section 2.1 and processed in DaVis 8.4. A multi-pass cross-correlation algorithm was applied to the double-frame sets using 48×48-pixel (3.2×3.2-mm) Gaussian interrogation windows with 75% overlap for the final pass. Universal outlier detection (Westerweel & Scarano 2005) was applied to the resulting vector fields to remove spurious vectors, which are estimated to account for less than 1% of the vectors in each stereoscopic snapshot. A sliding ensemble of correlation algorithm with a filter length of 5 images using 4 successive pairs was applied to the single-frame sets to reduce random, high-frequency noise (Ghaemi *et al.* 2012). The same interrogation

window parameters used for the double-frame processing were applied here, but no vector postprocessing was applied to the time-resolved sets due to a lack of outliers.

The uncertainty in the instantaneous wake PIV measurements has been estimated using linear propagation assuming that the uncertainty in displacement is 0.1 pix (Raffel *et al.* 2018) and that the uncertainty in the time between recorded frames is negligible. It then follows that the estimated uncertainty in the instantaneous measurements is at most $0.011U_\infty$ for any given measurement used here. The out-of-plane component of the stereoscopic measurements likely has a larger uncertainty, but this component was not employed in this investigation. Assuming independent samples, the uncertainty in the mean wake velocity fields is estimated to be at most $0.007U_\infty$. The uncertainty in Q-criterion (Jeong & Hussain 1995) is difficult to quantify because it not yet clear how calibration errors and the correlations between velocity components propagate for stereoscopic measurements (Sciacchitano & Wieneke 2016). However, we have used the error associated with the spatial derivatives to estimate that the uncertainty is on the order of $0.001Q_{\mathrm{max}}$ or $0.01Q_{\mathrm{mean}}$.

3. Results

3.1. *Upstream boundary layer development*

The properties of the upstream boundary layer have been investigated using the mean velocity fields computed within FOV2. The freestream velocity (U_∞), boundary layer thickness (δ_{99}), displacement thickness (δ), and momentum thickness (θ) are given in table 1 for all Re investigated with and without tripwires, all evaluated $3h$ upstream from the BTE ($x = -3h$). Mean velocity profiles at the same location are presented in figure 2(a) for selected laminar and turbulent cases, and the associated shape factors $H = \delta/\theta$ are plotted in figure 2(b). The shape factor estimates are affected by a lack of reliable data very close to the wall, but the trends still allow for visualization of boundary layer transition. The profiles were evaluated $3h$ upstream from the BTE because the wake induces a favourable pressure gradient that causes the boundary layer flow to accelerate, resulting in a bulge in the profile where velocities greater than U_∞ are observed. This flow acceleration was also reported by Gibeau *et al.* (2018), and it makes determining properties of the boundary layer such as δ_{99} difficult. The pressure gradient at $x = -3h$ is sufficiently weak such that the profiles can be properly evaluated. These profiles were compared to those at $x = -1h$ and it was found that the boundary layer state does not change significantly over this distance, i.e. the cases that are laminar or transitional at $x = -3h$ remain laminar or transitional at $x = -1h$.

Without tripwires, $Re(h) = 2600$ to 13200 feature a fully laminar upstream boundary layer as is indicated by the shape factors, after which the boundary layer begins to transition. The shape factors and visual inspection of the boundary layer profiles reveal that a fully turbulent boundary layer is not achieved at any Re for the untripped case, and this is due to the short chord length of the model. The addition of the tripwires causes transition to occur earlier, with only $Re(h) = 2600$ being fully laminar, and $13200 \leqslant Re(h) \leqslant 25800$ being fully turbulent. The tripped boundary layer is thicker in all cases (see table 1). As is visible in figure 2(a), the fully turbulent profile for the tripped case ($Re(h) = 25800$) agrees well with the 1/7 power law beyond $y/\delta_{99} \approx 0.1$. The untripped profile only agrees well beyond $y/\delta_{99} \approx 0.4$ because it has not yet become fully turbulent. Both $Re(h) = 2600$ profiles agree reasonably well with the Blasius profile. Figure 2(b) also contains the shape factors of the upstream boundary layer from Naghib-Lahouti
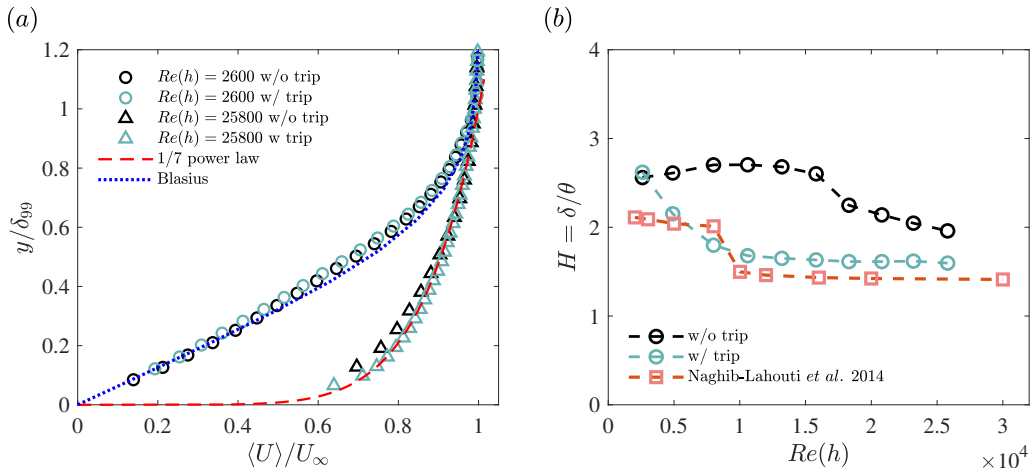
(a)

(b)

FIGURE 2. (a) Mean boundary layer profiles for sample cases of laminar and turbulent flow with and without tripwires at $x = -3h$ and (b) the associated shape factors $H = \delta/\theta$ showing when the transition to turbulence occurs.

et al. (2014). The boundary layer in their study can be seen to transition at a higher Re compared to the tripped case in the present investigation. This is expected because Naghib-Lahouti *et al.* (2014) utilized tripwires with half the size of the ones used here and therefore they would have caused a smaller disturbance.

In addition to knowing when the upstream flow transitions to turbulence, the boundary layer length scales are used for normalization purposes. A modified BTE height $h' = h + 2\delta$ can be defined using the upstream displacement thickness to estimate an effective trailing-edge height when investigating the wake at different Re. Both h and h' will be used for normalization purposes moving forward to facilitate comparison with the work of Naghib-Lahouti *et al.* (2012, 2014) and to study whether h' is an appropriate length scale for normalizing the results pertaining to the streamwise vortices. The location where the boundary layer properties were evaluated ($x = -3h$) is sufficiently close to the BTE for this purpose. The error associated with calculating h' using $\delta(c - 3h)$ instead of $\delta(c)$ has been estimated using the Blasius and 1/7 power law relations for the displacement thickness of the laminar and turbulent profiles, respectively. This analysis yielded a maximum error in h' of less than 3% as a result of evaluating the boundary layer properties at $x = -3h$ instead of at the BTE.

3.2. *Characteristics of the spanwise vortices*

The spanwise vortices are investigated here to compare the mean flow results with those of Naghib-Lahouti *et al.* (2012, 2014). This evaluation is necessary to justify direct comparison of the results in the next sections. The evaluation is conducted by comparing formation lengths (L_f), wavelengths of the spanwise vortices (λ_x), and vortex shedding frequencies (f_s). The latter is accomplished using the Strouhal number (St).

The formation length is defined as the length of the mean recirculation bubble in the wake. This has been calculated using the mean streamwise velocity along the wake centreline ($y = -0.5h$) from the 2C-PIV results in FOV3. Curves of centreline mean velocity $U_c(x)$ are plotted in figure 3(a) for all cases. The formation length was calculated by determining the point at which $U_c = 0$. The results have been normalized by h' and are plotted in figure 3(b) in comparison to those of Naghib-Lahouti *et al.* (2012, 2014).

$Re(h)$	U_∞ [m s^{-1}]	δ_{99} [mm]	δ [mm]	θ [mm]
2600	3.1	3.9, 4.0*	1.4, 1.5*	0.6, 0.6*
4900	5.9	2.9, 4.5*	1.1, 0.9*	0.4, 0.4*
8000	9.6	2.5, 5.2*	0.9, 0.7*	0.3, 0.4*
10600	12.8	2.2, 5.2*	0.8, 0.7*	0.3, 0.4*
13200	16.0	1.9, 5.1*	0.7, 0.7*	0.2, 0.4*
15800	19.1	1.7, 5.1*	0.6, 0.7*	0.2, 0.4*
18300	22.2	1.8, 4.9*	0.4, 0.7*	0.2, 0.4*
20800	25.2	2.2, 4.9*	0.4, 0.7*	0.2, 0.4*
23200	28.1	2.4, 4.8*	0.4, 0.7*	0.2, 0.4*
25800	31.2	2.6, 5.0*	0.4, 0.7*	0.2, 0.5*

TABLE 1. Parameters relating to the mean velocity profiles shown in figure 2(a). Values marked with * denote properties for the tripped cases.

L_f/h' for the tripped case is larger than L_f/h' for the untripped case for the first two Re, at which point the trend switches. This switch coincides with the upstream transition to turbulence for the tripped case. Beyond $Re(h') \approx 7000$, L_f/h' shows a slight downward trend with a nearly constant offset between the tripped and untripped results. This offset indicates that a thicker upstream boundary layer reduces L_f/h' in the wake after the upstream boundary layer has transitioned. The L_f/h' results of Naghib-Lahouti $et\ al.$ (2014) also show a slight reduction with increasing Re and their values generally agree with the present results as is clear in figure 3(b).

The vortex shedding frequency has been obtained by calculating the power spectral density of the fluctuating component of the streamwise velocity signal $u(t)$ in the wake from the 2C-PIV results in FOV3. The fluctuating signal was extracted at $(x, y) = (1.0h, 0.7h)$ according to the axes in figure 1. This point was selected to capture the large-scale fluctuations of the shed vortices without capturing the turbulent fluctuations that occur in the near-wake. Each spectrum consisted of a single peak and the location of each peak has been taken as the dominant vortex shedding frequency. The Strouhal number $St(h') = f_s h'/U_\infty$ has been calculated for all cases and plotted against $Re(h')$ in figure 3(c). The $St(h')$ values from Naghib-Lahouti $et\ al.$ (2014) for a fully laminar (0.289) and fully turbulent (0.231) upstream boundary layer are shown in the plot for comparison. It is first interesting to note that the trends in figure 3(c) are similar to those of the shape factors in figure 2(b), revealing that the state of the upstream boundary layer directly affects the vortex shedding frequency in the wake. When the present upstream boundary layer is fully laminar (the first Re is used), Strouhal numbers of $St(h') = 0.275$ and 0.268 are obtained with and without tripwires, respectively, corresponding to differences of at most 7% when compared to the result of Naghib-Lahouti $et\ al.$ (2014). Some modulation in $St(h')$ is visible in figure 3(c) for the present fully turbulent upstream cases. However, when compared to the result of Naghib-Lahouti $et\ al.$ (2014), all differences are less than 5%. We therefore conclude that the normalized shedding frequencies calculated in the present investigation agree with the results of Naghib-Lahouti $et\ al.$ (2014) within a few percent.

The wavelength of the spanwise vortices, defined as the distance between the vortices shed from one side of the BTE, is calculated as $\lambda_x = U_c/f_s$ where U_c is the mean centreline velocity sufficiently downstream from the BTE. The $U_c(x)$ results shown in figure 3(a) reveal asymptotic trends with increasing distance from the BTE. For the purposes of calculating λ_x, the final values shown in figure 3(a) are chosen as the value for U_c sufficiently downstream. This location is $x = 4h$, thus matching the location used
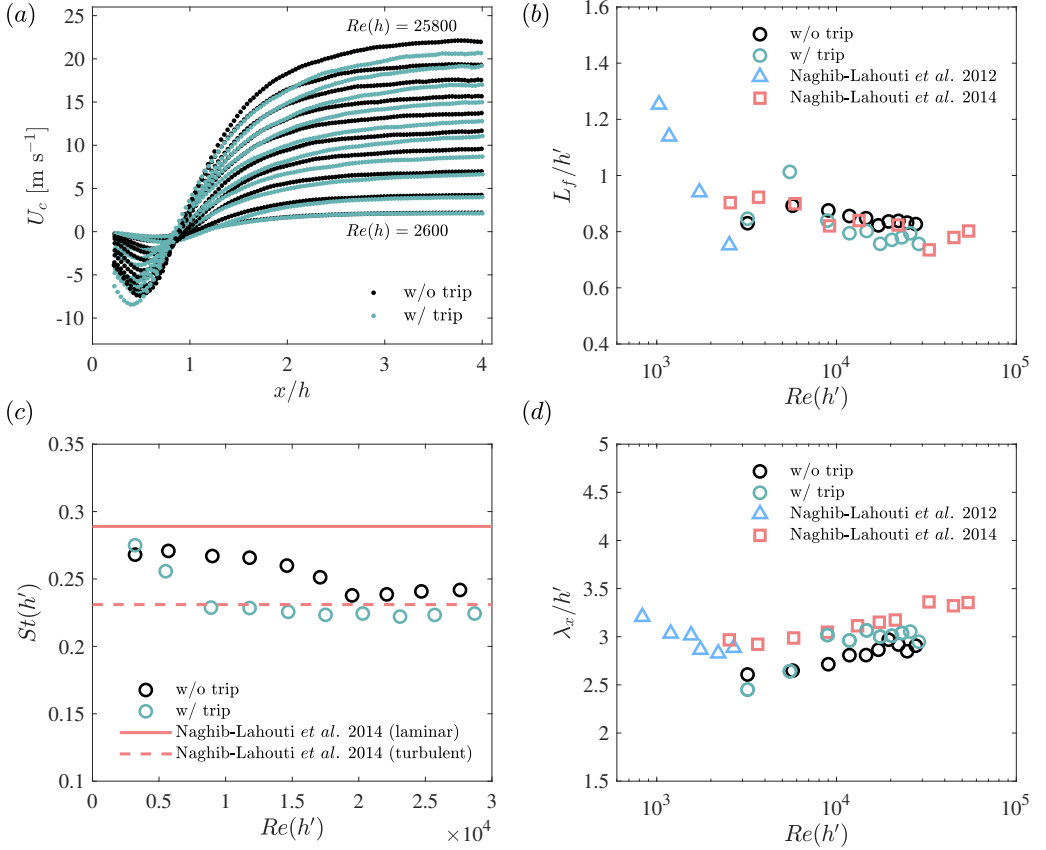
FIGURE 3. Characteristics of the spanwise vortices for comparison with Naghib-Lahouti *et al.* (2012, 2014): (*a*) mean centreline velocity U_c, (*b*) formation length L_f, (*c*) Strouhal number $St(h')$, and (*d*) wavelength of the spanwise vortices λ_x.

by Naghib-Lahouti *et al.* (2014) for the same calculation. The resulting values for λ_x/h' are plotted in figure 3(*d*) in comparison to those of Naghib-Lahouti *et al.* (2012, 2014). The trends increase with Re and show an opposite pattern to those of L_f/h', i.e. λ_x/h' for the untripped case is larger for the first two Re, followed by λ_x/h' for the tripped case being larger for the remainder with a near-constant offset between the values. Once again, the thicker upstream turbulent boundary layer appears to impact the spanwise vortices in the wake. Once the upstream boundary layer has transitioned, the present tripped results agree well with those of Naghib-Lahouti *et al.* (2014), who also employed a tripwire.

Considering the formations lengths, vortex shedding frequencies, and wavelength of spanwise vortices calculated here, we can conclude that the present flow field is in good agreement with those of Naghib-Lahouti *et al.* (2012, 2014) and therefore direct comparison of the streamwise vortex results is justified.

3.3. *Spanwise wavelength of the streamwise vortices*

The streamwise vortices are investigated here using the techniques of Gibeau *et al.* (2018). The stereo-PIV results within FOV4 were used to calculate the two-dimensional Q-criterion, for which $Q > 0$ denotes a vortex and all $Q < 0$ are discarded. A second-order

central differencing scheme was employed to estimate the spatial derivatives. Vorticity was not used to identify vortex cores here because the flow under investigation features high shear, which has the potential to mask the vortical structures when vorticity is applied. Q-criterion is capable of extracting local rotation in the presence of high shear and identifies the same structures as the commonly used λ_2-criterion in the two-dimensional case (Jeong & Hussain 1995). However, Q-criterion does not distinguish between directions of rotation. The Q-criterion has therefore been modified to account for direction of rotation using the sign of vorticity; we define this modified Q-criterion as $Q' = \omega_x Q/|\omega_x|$. This is done to properly capture the counter-rotating streamwise vortex pairs. Sample snapshots of Q' are presented in figure 4 for all Re from the untripped data set. A small-scale streamwise vortex structure with alternating Q' in the spanwise direction is visible in all cases. Note that these snapshots were chosen to represent the streamwise vortices when the wake is more organized, as large-scale abnormalities tend to distort the wake, especially as Re is increased. These wake distortions are due to oblique vortex shedding (Williamson 1989), vortex dislocations (Williamson 1992), and cellular vortex shedding (Scarano & Poelma 2009). An example of the latter is shown in the subplot for $Re(h) = 25800$ in figure 4, where the spanwise row of streamwise vortex pairs has been distorted as a result of two adjacent cells shedding out-of-phase. Despite large-scale wake distortions being prevalent, streamwise vortex pairs clearly exist in all snapshots of Q'.

The wavelength of the streamwise vortices (λ_z) is determined statistically by applying a spanwise autocorrelation to the snapshots of Q'. The autocorrelation coefficient is defined for the ith snapshot by

$$C(\Delta z) = \frac{\langle Q'(y_0, z_0, t_i) \cdot Q'(y_0, z_0 + \Delta z, t_i) \rangle}{Q'_{rms}(y_0, z_0, t_i)^2} \tag{3.1}$$

where Δz denotes a shift in the spanwise direction and the subscript rms indicates the application of the root-mean-square operation. The result is an autocorrelation curve as a function of Δz for each snapshot. The spanwise distance between adjacent vortex pairs within a snapshot is then taken as twice the distance between the initial maximum of the autocorrelation curve ($C(0) = 1$) and the first local minimum, which is typically negative. This is because the first minimum occurs where Δz aligns vortices with opposite signs of rotation and therefore it represents half the distance between vortex pairs.

Applying equation 3.1 to all uncorrelated snapshots results in a distribution of λ_z for each Re, with and without tripwires. These distributions can be used to determine the mean and most probable values for λ_z. A histogram based on the 2700 autocorrelation curves for $Re(h) = 2600$, untripped, is presented in figure 5(a). This distribution is unimodal and right-skewed. The single peak suggests that there is only one dominant wavelength present in the wake, and this remains true for the other 19 cases considered. While the mean of this distribution can be calculated using the histogram, the most probable value (i.e. the mode) is biased because it depends on the chosen histogram bin size. This problem is alleviated by fitting each histogram with a probability density function (PDF). A Burr type XII distribution (Tadikamalla 1980) was chosen for its ability to represent positive, unimodal distributions. Sample PDFs for $Re(h) = 2600$ and 25800, both with and without tripwires, are presented in figure 5(b). First, when comparing the histogram in figure 5(a) with the associated curve in figure 5(b) for $Re(h) = 2600$, it is evident that the fit PDF represents the distribution well. Second, it can be seen that the addition of tripwires does not significantly affect the PDFs. Finally, the distributions reduce in height and broaden slightly as Re is increased, and all PDFs
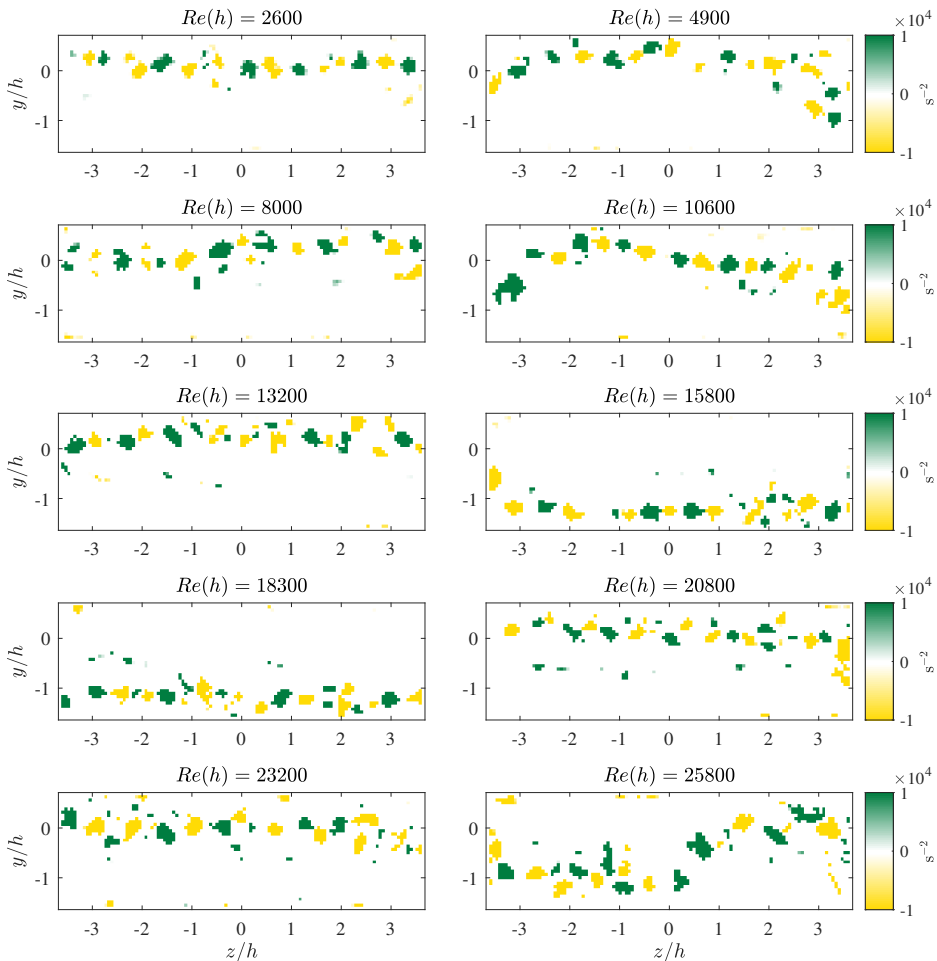
FIGURE 4. Snapshots of the modified Q-criterion ($Q' = \omega_x Q/|\omega_x|$) in the wake at $x = 2h$ for all Re; from the uncorrelated and untripped data set.

fall between the two extremes shown in figure 5(b). Note that the values captured by these distributions agree with visual inspection of the wavelengths in figure 4.

The most probable values ($\widetilde{\lambda}_z$) from all PDFs have been extracted and are plotted in figure 6(a) in comparison to the results of Gibeau *et al.* (2018), normalized using both h and h'. The smallest and largest values for $\widetilde{\lambda}_z$ occur at $Re(h) = 2600$ and 25800 for the tripped case and correspond to $0.67h$ and $0.85h$, respectively. The trends of $\widetilde{\lambda}_z$ appear to increase asymptotically for both normalizations, with and without tripwires, although the asymptote is reached later for the h' normalization. There is no clear relationship between the tripped and untripped cases when the h' normalization is used, but normalization with h reveals a relationship that matches that of the wavelength of the spanwise vortices. More specifically, $\widetilde{\lambda}_z/h$ for the untripped case is larger for the first two Re, followed by $\widetilde{\lambda}_z/h$ for the tripped case being larger for the remainder with a slight offset between the values. However, these differences are small and may not be significant. Comparison with Gibeau *et al.* (2018) shows good agreement with the present results, with the best agreement occurring when the h normalization is used. This is despite the large AR of
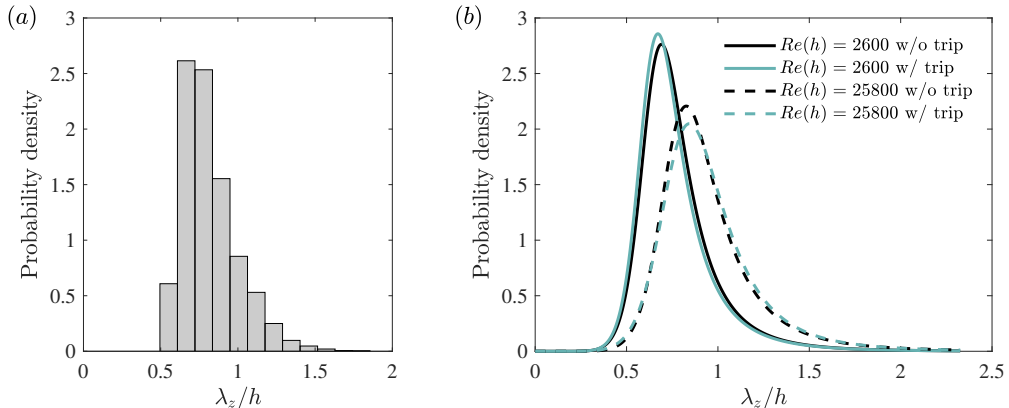
FIGURE 5. (*a*) Sample histogram of the wavelength of the streamwise vortices (λ_z) at $Re(h) = 2600$ without tripwires and (*b*) the fit probability density functions of λ_z at the lowest and highest Re with and without tripwires.
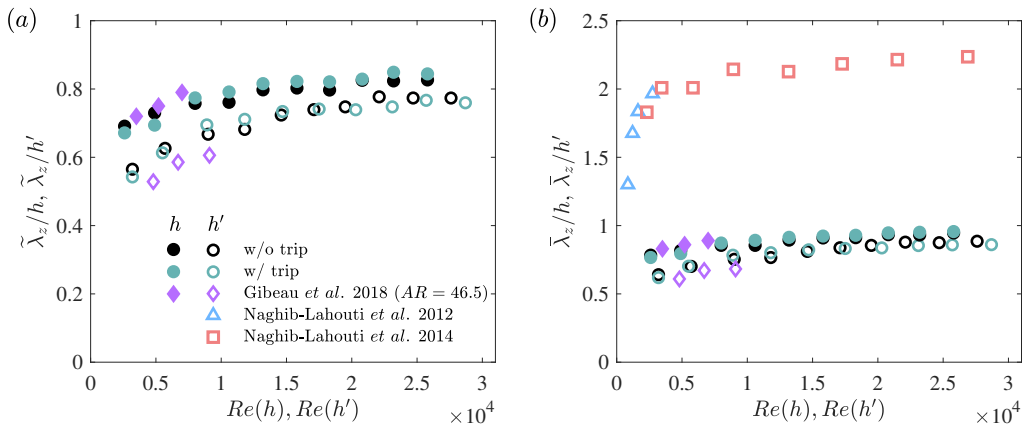

FIGURE 6. (*a*) The modes (i.e. most probable values) of the wavelength of the streamwise vortices (λ_z) normalized by both h and h' for all cases and (*b*) the mean values of λ_z normalized by both h and h' for all cases.

46.5 used within their study. Direct comparison with Naghib-Lahouti *et al.* (2012, 2014) is not possible here because they did not report the most probable λ_z or distributions of λ_z in their work.

The mean values ($\bar{\lambda}_z$) from all PDFs are plotted in figure 6(*b*) in comparison to the results of Gibeau *et al.* (2018) and Naghib-Lahouti *et al.* (2012, 2014), normalized using both h and h'. The present results for $\bar{\lambda}_z$ also appear to increase asymptotically, with the steeper trend occurring for the h' normalization. The smallest and largest values once again occur at $Re(h) = 2600$ and 25800 for the tripped case and correspond to $0.77h$ and $0.96h$, respectively. Good agreement with the results of Gibeau *et al.* (2018) for $AR = 46.5$ is evident, with the best agreement occurring when the h normalization is used. No agreement with the results of Naghib-Lahouti *et al.* (2012, 2014) is found. As was discussed in the introduction and shown by Gibeau *et al.* (2018), this is likely due to the low-pass filtering effect of the reduced-order model obtained from proper orthogonal decomposition, which altered the wavelength of the streamwise vortices. The present
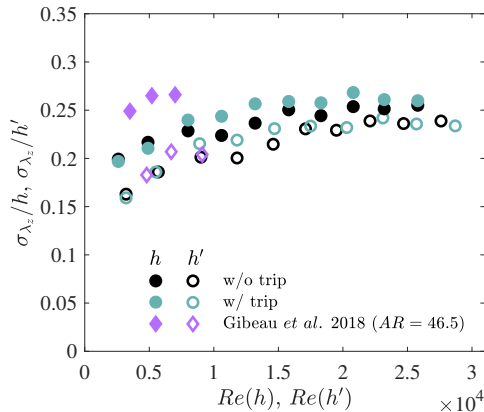
FIGURE 7. Standard deviations of the wavelength of streamwise vortices (σ_{λ_z}) normalized by both h and h' for all cases.

direct measurements of the streamwise vortices show that a small-scale streamwise vortex structure with a mean wavelength approaching roughly $1h$ is present in the wake for all Re considered here.

The distributions of λ_z shown in figure 5(b) are relatively wide for all Re. This is likely due to wake distortion caused by the previously mentioned oblique vortex shedding, vortex dislocations, and cellular vortex shedding. It is also important to note that the lowest Re considered here is an order of magnitude higher than the secondary instability transition point, and so it is unlikely that the streamwise vortex pairs would remain highly organized at these Re. To investigate the width of the distributions, the standard deviations of λ_z, denoted as σ_{λ_z}, have been computed from the distributions and are plotted for all cases in figure 7, normalized by both h and h' and compared to the results of Gibeau *et al.* (2018). Similarly to the results for $\widetilde{\lambda}_z$ and $\bar{\lambda}_z$, the trends for σ_{λ_z} appear to increase asymptotically. The trends indicate that the tripped upstream turbulent boundary layer results in a larger σ_{λ_z}/h for $Re(h) \geqslant 8000$, which is visible as an offset between the two trends. The offset is no longer visible for the highest Re when the h' normalization is applied, suggesting that σ_{λ_z} is dependent on the properties of the upstream boundary layer. This observation is strengthened when considering the results of Gibeau *et al.* (2018), which show poor agreement with the present results for σ_{λ_z}/h but good agreement for σ_{λ_z}/h'. This is in contrast to the results for λ_z (figure 6), which show better agreement when h is used to normalize. Considered together, these observations indicate that σ_{λ_z} has a stronger dependence than λ_z on the state of the upstream boundary layer.

3.4. *Temporal behaviour of the streamwise vortices*

The wavelength of the streamwise vortices measured here could correspond to the mode B structure found in the wakes of circular cylinders (Williamson 1996a), square cylinders (Luo *et al.* 2007), and highly-elongated blunt bodies (Gibeau *et al.* 2018), or it could correspond to the predicted mode S′ (Ryan *et al.* 2005). The difference depends on whether the streamwise vortex pairs maintain their directions of rotation over time (mode B) or change their direction every full shedding cycle of the spanwise vortices (mode S′). This is first investigated qualitatively using the time-resolved measurements of Q' in the wake at $x = 2h$. Three-dimensional isosurface constructions of the structures in the wake have been obtained by stacking the time-resolved, two-dimensional measurements along the
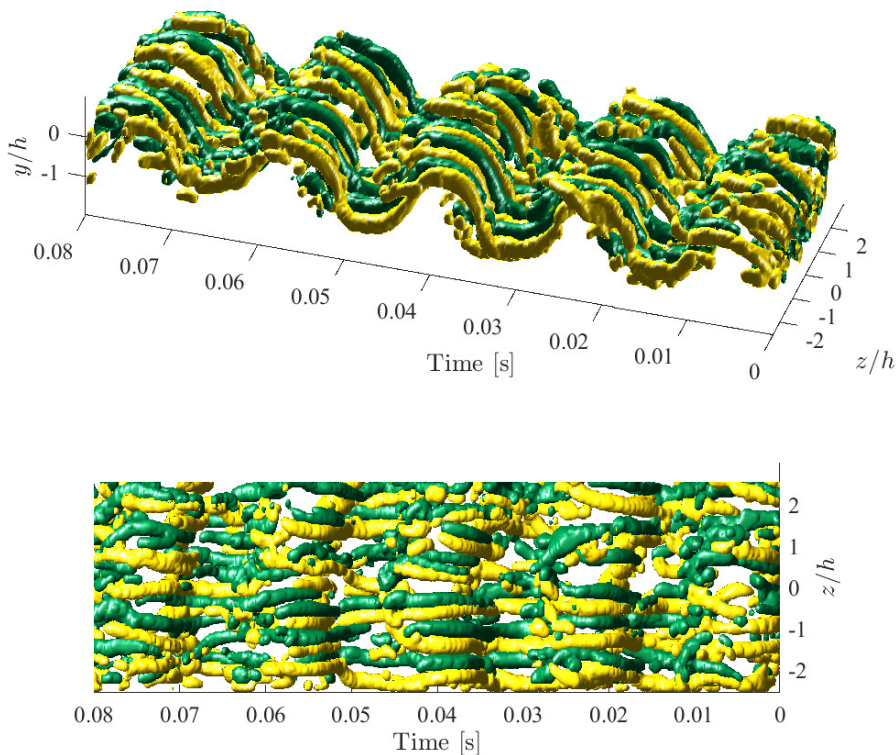
FIGURE 8. Isosurface construction of modified Q-criterion ($Q' = \omega_x Q/|\omega_x|$) in the wake at $x = 2h$ for $Re(h) = 2600$ without tripwires. Green and gold represent positive and negative rotational directions, respectively. The isosurface was set to $Q' = \pm 1500$ s^{-2}. A second-order regression filter with a kernel size of 3 has been applied to the data to reduce noise.

temporal dimension. A sample construction of the structures is shown in figure 8 for $Re(h) = 2600$, untripped. The alternating sign of vorticity in the spanwise direction is clearly visible, and the streamwise vortices in the figure can be seen to maintain their directions of rotation over several shedding cycles. This indicates that mode B is present in the wake, and this visualization agrees with the mode B constructions presented by Brede *et al.* (1996) in the wake of a circular cylinder and Gibeau *et al.* (2018) in the wake of an elongated blunt body with $AR = 46.5$. However, this qualitative analysis only captures a small number of vortex shedding cycles. A statistical analysis is necessary to say whether mode B is persistent in the wake.

  Whether the streamwise vortex pairs maintain their directions of rotation over time can be statistically investigated by applying a cross-correlation analysis to the temporal constructions of Q'. The measurements of Q' from individual vortex shedding cycles are isolated as three-dimensional matrices and successive shedding cycles are cross-correlated in the spanwise direction. If the streamwise vortices maintain their directions of rotation, the cross-correlation curve will begin at a positive value because vortices with the same directions of rotation will align. The spanwise shift will then cause the correlation curve to reduce to a minimum value at roughly $\Delta z = 0.5\lambda_z$ where vortices with opposite directions of rotation align. The opposite will be true if the streamwise vortex pairs change their direction of rotation during shedding cycles. Specifically, the cross-correlation curve will begin at a minimum and trend towards a maximum at approximately $\Delta z = 0.5\lambda_z$. This

operation can be conducted for all N available vortex shedding cycles and the resulting curves can be averaged as described by

$$\rho(\Delta z) = \frac{1}{N-1} \sum_{i=1}^{N-1} \frac{\langle Q'(y_0, z_0, t_i) \cdot Q'(y_0, z_0 + \Delta z, t_i + T_{shed}) \rangle}{Q'_{rms}(y_0, z_0, t_i) Q'_{rms}(y_0, z_0, t_i + T_{shed})} \tag{3.2}$$

where Q' is a three-dimensional matrix containing a full shedding cycle and T_{shed} represents the period of the primary shedding cycle. Equation 3.2 can only be applied when the data is sufficiently time-resolved and relatively organized, as large-scale wake distortions corrupt the cross-correlation. For example, oblique vortex shedding (Williamson 1989) causes the streamwise vortices to align at an angle with respect to the freestream direction, thus imposing a shift in the streamwise vortices between primary shedding cycles. Because of this, the cross-correlation analysis can only be applied at low Re, as large-scale wake distortions and a lack of sufficiently time-resolved data become problematic when Re is increased.

The result of applying equation 3.2 to the time-resolved stereo-PIV data is shown in figure 9 for $Re(h) = 2600$, 4900, and 8000, with and without tripwires. The cross-correlation was applied to a segment of the data spanning $4h$ to improve the correlations in the presence of the large-scale wake distortions. This is the same spanwise extent of the data shown in figure 8. The cross-correlation curves for $Re(h) = 2600$ both begin at a positive maximum and trend towards minimums, indicating that mode B is persistent in the wake. These minimums occur at roughly $\Delta z = 0.4h$ and therefore agree with the mean wavelength of the streamwise vortices reported in figure 6(b). The curves for $Re(h) = 4900$ and 8000 also begin at positive maximums and trend downwards. However, with the exception of one case, the minimums are not as clear since the correlation is much weaker. This is the result of the previously mentioned large-scale wake distortions and the increased turbulence associated with high Re, which also explains the generally small magnitudes of the cross-correlation coefficients. Because of this, we cannot prove that the streamwise vortex pairs maintain their directions of rotation at higher Re. However, secondary instability transitions are generally a low-Re phenomenon. Both Ryan *et al.* (2005) and Naghib-Lahouti *et al.* (2012) suggested mode B′ for low Re, and a further transition to mode B at higher Re was not discussed.

4. Summary and Conclusions

This work was motivated by the observation of different streamwise vortex structures in the wake of a body with $AR = 12.5$ by Ryan *et al.* (2005) and Naghib-Lahouti *et al.* (2012, 2014) in comparison to the results of Gibeau *et al.* (2018) for $AR = 46.5$. The latter authors also suggested that the mode B′ reported by Naghib-Lahouti *et al.* (2012, 2014) may not be physical, but the result of retaining insufficient energy during their POD reconstruction. Here we experimentally investigate the streamwise vortices in the wake of an elongated blunt body with $AR = 12.5$ using particle image velocimetry for $2600 \leqslant Re(h) \leqslant 25800$ where h is the height of the blunt trailing edge (BTE).

The spanwise vortices were first compared to those of Naghib-Lahouti *et al.* (2012, 2014). The formation lengths, vortex shedding frequencies, and wavelength of the spanwise vortices were found to be in good agreement between studies. The wavelength of the streamwise vortices in the wake was then determined statistically using an autocorrelation technique. The most probable values ranged from $0.67h$ to $0.85h$, and the mean values ranged from $0.77h$ to $0.96h$, both appearing to increase asymptotically with Re. The abrupt transition of the upstream boundary layer, induced using tripwires, was found to
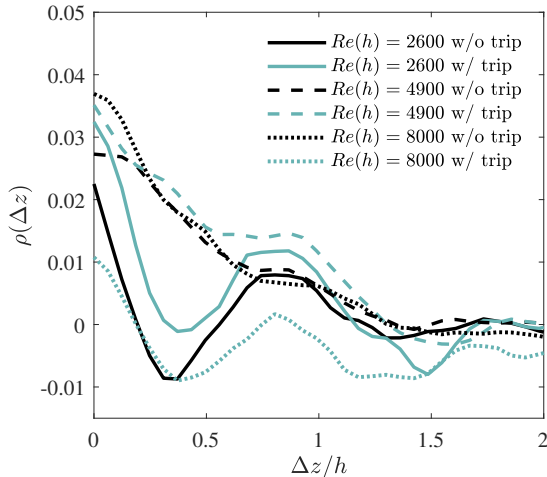
FIGURE 9. Cross-correlation coefficient calculated using equation 3.2 for $Re(h) = 2600$, 4900, and 8000, with and without tripwires.

slightly increase the wavelength of the streamwise vortices. The streamwise vortices were then shown to maintain their directions of rotation during primary shedding cycles at low Re by visually inspecting isosurfaces of a modified Q-criterion and using cross-correlations applied to successive shedding cycles. The observed wavelength and continuous direction of rotation of the streamwise vortices indicates that mode B is present in the wake.

Past work has revealed the mode B structure in the wake of a highly elongated blunt body with $AR = 46.5$ (Gibeau *et al.* 2018) as well as in the wakes of square cylinders, i.e. $AR = 1$ (Luo *et al.* 2007; Tong *et al.* 2008). The current results reveal the presence of streamwise vortices that are consistent with mode B in the wake of a body with $AR = 12.5$. These conclusions suggest that aspect ratio may not play an important role in the formation of the streamwise vortices. However, further investigation into a wider range of AR and Re is needed to confirm this.

The spanwise scaling of mode B in the wake of a BTE as it relates to AR is not clear. The development of the upstream boundary layer as a result of larger AR does not seem to greatly affect the wavelength of the streamwise vortices because the best collapse of the data is observed when h is used for normalization. However, the standard deviation of wavelengths found in the wake seems to scale better with h', suggesting that upstream boundary layer development has some impact. A small jump in the wavelength of the streamwise vortices is also observed when the tripped upstream boundary layer transitions to turbulence, suggesting that the state of the upstream boundary layer (laminar or turbulent) also has some effect. Further investigation is required to determine exactly how AR affects mode B in the wake, as these observations are based on limited data collected from a single facility.

Acknowledgements

REFERENCES

Baker, J. P., Mayda, E. A. & van Dam, C. P. 2006 Experimental analysis of thick blunt trailing-edge wind turbine airfoils. *J. Sol. Energy Eng.* **128** (4), 422–431.

Barkley, D. & Henderson, R. D. 1996 Three-dimensional Floquet stability analysis of the wake of a circular cylinder. *J. Fluid Mech.* **322**, 215–241.

Bays-Muchmore, B. & Ahmed, A. 1993 On streamwise vortices in turbulent wakes of cylinders. *Phys. Fluids A* **5** (2), 387–392.

Berger, E. & Wille, R. 1972 Periodic flow phenomena. *Annu. Rev. Fluid Mech.* **4**, 313–340.

Blackburn, H. M. & Lopez, J. M. 2003 On three-dimensional quasiperiodic Floquet instabilities of two-dimensional bluff body wakes. *Phys. Fluids* **15** (8), L57.

Blackburn, H. M., Marques, F. & Lopez, J. M. 2005 Symmetry breaking of two-dimensional time-periodic wakes. *J. Fluid Mech.* **522**, 395–411.

Brede, M., Eckelmann, H. & Rockwell, D. 1996 On secondary vortices in the cylinder wake. *Phys. Fluids* **8** (8), 2117–2124.

Gerrard, J. H. 1978 The wakes of cylindrical bluff bodies at low Reynolds number. *Phil. Trans. R. Soc. A* **288** (1354), 351–382.

Ghaemi, S., Ragni, D. & Scarano, F. 2012 PIV-based pressure fluctuations in the turbulent boundary layer. *Exp. Fluids* **53** (6), 1823–1840.

Gibeau, B., Koch, C. R. & Ghaemi, S. 2018 Secondary instabilities in the wake of an elongated two-dimensional body with a blunt trailing edge. *J. Fluid Mech.* **846**, 578–604.

Gibeau, B., Koch, C. R. & Ghaemi, S. 2019 Active control of vortex shedding from a blunt trailing edge using oscillating piezoelectric flaps. *Phys. Rev. Fluids* **4**, 054704.

Jeong, J. & Hussain, F. 1995 On the identification of a vortex. *J. Fluid Mech.* **285**, 69–94.

Jethani, Y., Kumar, K., Sameen, A. & Mathur, M. 2018 Local origin of mode-B secondary instability in the flow past a circular cylinder. *Phys. Rev. Fluids* **3**, 103902.

Johnson, M. R. & Kostiuk, L. W. 2000 Efficiencies of low-momentum jet diffusion flames in crosswinds. *Combust. Flame* **123** (1), 189–200.

Luo, S. C., Tong, X. H. & Khoo, B. C. 2007 Transition phenomena in the wake of a square cylinder. *J. Fluids Struct.* **23** (2), 227–248.

Mansy, H., Yang, P. M. & Williams, D. R. 1994 Quantitative measurements of three-dimensional structures in the wake of a circular cylinder. *J. Fluid Mech.* **270**, 277–296.

Meinhart, C. D., Wereley, S. T. & Santiago, J. G. 2000 A PIV algorithm for estimating time-averaged velocity fields. *J. Fluids Eng.* **122** (2), 285–289.

Naghib-Lahouti, A., Doddipatla, L. S. & Hangan, H. 2012 Secondary wake instabilities of a blunt trailing edge profiled body as a basis for flow control. *Exp. Fluids* **52** (6), 1547–1566.

Naghib-Lahouti, A., Lavoie, P. & Hangan, H. 2014 Wake instabilities of a blunt trailing edge profiled body at intermediate Reynolds numbers. *Exp. Fluids* **55** (7), 1779.

Ng, Z. Y., Vo, T. & Sheard, G. J. 2018 Stability of the wakes of cylinders with triangular cross-sections. *J. Fluid Mech.* **844**, 721–745.

Oertel, H. 1990 Wakes behind blunt bodies. *Annu. Rev. Fluid Mech.* **22**, 539–564.

Petrusma, M. S. & Gai, S. L. 1996 Bluff body wakes with free, fixed, and discontinuous separation at low Reynolds numbers and low aspect ratio. *Exp. Fluids* **20** (3), 189–198.

Raffel, M., Willert, C. E., Scarano F., Kähler, C., E., C., Wereley, S. T. & Kompenhans, J. 2018 *Particle Image Velocimetry: A Practical Guide*. Berlin, Germany: Springer.

Robichaux, J., Balachandar, S. & Vanka, S. P. 1999 Three-dimensional Floquet instability of the wake of square cylinder. *Phys. Fluids* **11** (3), 560–578.

Roshko, A. 1954 On the development of turbulent wakes from vortex streets. *NACA rep. 1191* .

Ryan, K., Thompson, M. C. & Hourigan, K. 2005 Three-dimensional transition in the wake of bluff elongated cylinders. *J. Fluid Mech.* **538**, 1–29.

Scarano, F. & Poelma, C. 2009 Three-dimensional vorticity patterns of cylinder wakes. *Exp. Fluids* **47** (1), 69–83.

Sciacchitano, A. & Wieneke, B. 2016 Piv uncertainty propagation. *Meas. Sci. Technol.* **27**, 084006.

Sheard, G. J., Fitzgerald, M. J. & Ryan, K. 2009 Cylinders with square cross-section: wake instabilities with incidence angle variation. *J. Fluid Mech.* **630**, 43–69.

Standish, K. J. & van Dam, C. P. 2003 Aerodynamic analysis of blunt trailing edge airfoils. *J. Sol. Energy Eng.* **125** (4), 479–487.

Tadikamalla, P. R. 1980 A look at the Burr and related distributions. *Int. Stat. Rev.* **48** (3), 337–344.

Thompson, M. C., Leweke, T. & Williamson, C. H. K. 2001 The physical mechanism of transition in bluff body wakes. *J. Fluids Struct.* **15** (3), 607–616.

Tong, X. H., Luo, S. C. & Khoo, B. C. 2008 Transition phenomena in the wake of an inclined square cylinder. *J. Fluids Struct.* **24**, 994–1005.

Wei, T. & Smith, C. R. 1986 Secondary vortices in the wake of circular cylinders. *J. Fluid Mech.* **169**, 513–533.

Westerweel, J. & Scarano, F. 2005 Universal outlier detection for PIV data. *Exp. Fluids* **39** (6), 1096–110.

Wieneke, B. 2005 Stereo-PIV using self-calibration on particle images. *Exp. Fluids* **39** (2), 267–280.

Williamson, C. H. K. 1988 The existence of two stages in the transition to three-dimensionality of a cylinder wake. *Phys. Fluids* **31** (11), 3165–3168.

Williamson, C. H. K. 1989 Oblique and parallel modes of vortex shedding in the wake of a circular cylinder at low Reynolds numbers. *J. Fluid Mech.* **206**, 579–627.

Williamson, C. H. K. 1992 The natural and forced formation of spot-like 'vortex dislocations' in the transition of a wake. *J. Fluid Mech.* **243**, 393–441.

Williamson, C. H. K. 1996*a* Three-dimensional wake transition. *J. Fluid Mech.* **328**, 345–407.

Williamson, C. H. K. 1996*b* Vortex dynamics in the cylinder wake. *Annu. Rev. Fluid Mech.* **28**, 477–539.

Wu, J., Sheridan, J., Welsh, M. C. & Hourigan, K. 1996 Three-dimensional vortex structures in a cylinder wake. *J. Fluid Mech.* **312**, 201–222.

Yildirim, I., Rindt, C. C. M. & van Steenhoven, A. A. 2013 Mode C flow transition behind a circular cylinder with a near-wake wire disturbance. *J. Fluid Mech.* **727**, 30–55.

Yoon, D. H., Yang, K. S. & Choi, C. B. 2010 Flow past a square cylinder with an angle of incidence. *Phys. Fluids* **22**, 043603.

Zhang, H. Q., Fey, U., Noack, B. R., König, M. & Eckelmann, H. 1995 On the transition of the cylinder wake. *Phys. Fluids* **7** (4), 779–794.